

000 001 002 003 004 005 006 007 008 009 010 011 012 013 014 015 016 017 018 019 020 021 022 023 024 025 026 027 028 029 030 031 032 033 034 035 036 037 038 039 040 041 042 043 044 045 046 047 048 049 050 051 052 053 ERROR PROPAGATION MECHANISMS AND COMPENSA- TION STRATEGIES FOR QUANTIZED DIFFUSION MOD- ELS

006
007 **Anonymous authors**
008 Paper under double-blind review

010 011 ABSTRACT

012
013 Diffusion models have transformed image synthesis by establishing unprece-
014 dented quality and creativity benchmarks. Nevertheless, their large-scale deploy-
015 ment faces challenges due to computationally intensive iterative denoising pro-
016 cesses. Although post-training quantization (PTQ) provides an effective pathway
017 for accelerating sampling, the iterative nature of diffusion models causes step-
018 wise quantization errors to accumulate progressively during generation, inevitably
019 compromising output fidelity. To address this challenge, we develop a theoretical
020 framework that mathematically formulates error propagation in Diffusion Models
021 (DMs), deriving per-step quantization error propagation equations and establish-
022 ing the first closed-form solution for cumulative error. Building on this theo-
023 retical foundation, we propose a timestep-aware cumulative error compensation
024 scheme. Extensive experiments on multiple image datasets demonstrate that our
025 compensation strategy effectively mitigates error propagation, significantly en-
026 hancing existing PTQ methods. Specifically, it achieves a 1.2 PSNR improvement
027 over SVDQuant on SDXL W4A4, while incurring only an additional $< 0.5\%$ time
028 overhead.

029 1 INTRODUCTION

030
031 DMs (Podell et al., 2023; Chen et al., 2024) have established themselves as highly effective deep
032 generative frameworks across diverse domains, including image synthesis (Ho et al., 2020), video
033 creation (Yang et al., 2024) and image translation (Sasaki et al., 2021) etc. Compared with con-
034 ventional SOTA generative adversarial networks (GANs), DMs exhibit superior stability, free from
035 the common pitfalls of model collapse and posterior collapse, which ensures more reliable and di-
036 verse output generation. Although diffusion models demonstrate remarkable capabilities in generat-
037 ing high-fidelity and diverse images, their substantial computational and memory overhead hinders
038 widespread adoption. This complexity primarily stems from two factors: first, the reliance on com-
039 plex deep neural networks (DNNs) for noise estimation; second, the requirement for an iterative
040 progressive denoising process to maintain synthesis quality, which may involve up to 1,000 iterative
041 steps, substantially increasing computational demands.

042 To address the substantial computational demands of noise estimation in diffusion models, re-
043 searchers employ quantization techniques to accelerate inference across all denoising steps. Depend-
044 ing on whether they require fine-tuning, quantization methods can be categorized into Quantization-
045 Aware Training (QAT) (Wu et al., 2020) and PTQ (Cai et al., 2020). QAT necessitates retraining
046 neural networks with simulated quantization and hyperparameter optimization, which introduces
047 significant computational overhead and deployment complexity, making it unsuitable for compute-
048 intensive diffusion model training. In contrast, PTQ directly derives quantization correction coeffi-
049 cients through calibration data statistics, thus avoiding the high-cost retraining process inherent to
050 diffusion models. Although PTQ has been widely studied in traditional vision tasks such as im-
051 age classification and object detection (Bhalgat et al., 2020), it faces many different challenges in
052 diffusion models. The architectural characteristics and training strategies of diffusion models in-
053 herently lead to the widespread presence of outliers in weight distributions, while activation values
054 exhibit step-wise distributional variations across time steps (Li et al., 2023a). These properties pose
055 significant challenges for quantization by inducing substantial step-wise error. Furthermore, the iter-

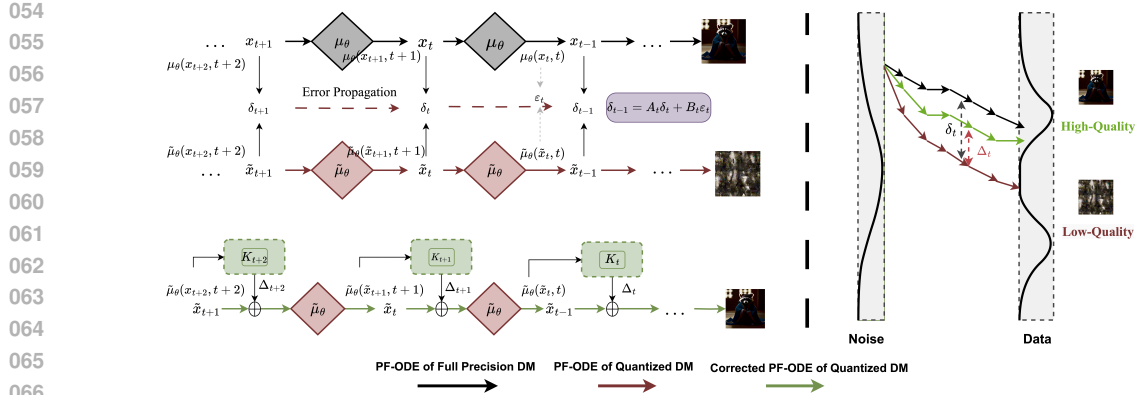


Figure 1: Visualization of Error Propagation and Correction in Quantized Diffusion Models. The gray path represents the iterative denoising process of the full-precision model μ , while the brown path represents that of the quantized model $\tilde{\mu}$. Affected by cumulative errors δ_t , its output gradually deviates from μ . The green path represents the denoising process after online correction of cumulative errors, with outputs better aligned with the full-precision model.

active denoising mechanism amplifies error accumulation across successive steps, where quantization errors progressively accumulate during the sampling trajectory, ultimately degrading generation fidelity. Recent advancements in PTQ (Wu et al., 2024; Li et al., 2023a; Zhao et al., 2024b) have predominantly focused on minimizing quantization errors at individual denoising steps. However, these approaches systematically neglect the critical analysis of error propagation dynamics throughout the iterative sampling trajectory. Consequently, current solutions (Li et al., 2024b) remain constrained to 4-bit quantization of both weights and activations while maintaining acceptable quality degradation, as cumulative errors across sequential denoising stages fundamentally limit lower-bit quantization viability.

Contrarily, our work focuses on the quantization error propagation problem in diffusion models and proposes the first timestep-aware cumulative error compensation scheme, called **TCEC**. First, we construct an error propagation equation by taking the DDIM (Song et al., 2020) as a paradigmatic case, presenting the field’s inaugural closed-form solution for cumulative error. However, direct computation of cumulative errors proves computationally infeasible. Subsequently, through the implementation of timestep-sensitive online rapid estimation for per-step quantization error, we achieve a notable simplification of the computational complexity inherent in cumulative error modeling. Finally, as shown in Figure 1, we incorporate a cumulative error correction term in each generation step, dynamically mitigating errors induced by quantization. In summary, our contributions are:

- We experimentally demonstrate that cumulative error is the primary cause of poor performance in low-precision DMs, thus presenting TCEC in response. Unlike conventional PTQ methods, TCEC directly computes cumulative errors and integrates correction terms during the iterative sampling process to align the outputs of quantized models with their floating-point counterparts.
- To accurately compute cumulative errors, we present a theoretical framework encompassing three key components: per-step quantization error, cumulative error, and error propagation. For the first time in the field, we derive a closed-form solution for cumulative error. Through rational approximations, we substantially simplify its computational complexity, enabling low-cost and rapid correction of cumulative errors.
- Extensive experiments across various diffusion models demonstrate our method’s effectiveness. TCEC-W4A4 reduces the memory footprint by $3.5\times$ compared to the FP16 model and accelerates inference by $3\times$ versus NF4 weight-only quantization, with engineering performance comparable to SVDQuant (Li et al., 2024b). Across all precision levels, it achieves superior image fidelity and diversity—for example, an sDCI PSNR \uparrow of 21.9 (vs. 20.7) and an MJHQ FID \downarrow of 18.1 (vs. 20.6).

108 Notably, TCEC maintains orthogonality to existing state-of-the-art PTQ algorithms (Li et al., 2024b;
 109 Zhao et al., 2024a) that minimize per-step quantization errors. Additionally, TCEC originates from
 110 rigorous theoretical derivation, and while its derivation process uses DDIM as an example, it is
 111 equally applicable to other solvers such as DPM++ (Lu et al., 2022).
 112

113 2 RELATED WORK

115 2.1 DIFFUSION MODEL

117 Diffusion models are a family of probabilistic generative models that progressively destruct real
 118 data by injecting noise, then learn to reverse this process for generation, represented notably by
 119 denoising diffusion probabilistic models (DDPMs) (Ho et al., 2020). DDPM is composed of two
 120 Markov chains of T steps. One is the forward process, which incrementally adds Gaussian noises
 121 into real sample $x_0 \in q(x_0)$, In this process, a sequence of latent variables $x_{1:T} = [x_1, x_2, \dots, x_T]$
 122 are generated in order and the last one x_T will approximately follow a standard Gaussian:

$$123 \quad q(\mathbf{x}_t \mid \mathbf{x}_{t-1}) = \mathcal{N}(\mathbf{x}_t; \sqrt{1 - \beta_t} \mathbf{x}_{t-1}, \beta_t \mathbf{I}) \quad (1)$$

125 where β_t is the variance schedule that controls the strength of the Gaussian noise in each step.
 126 The reverse process removes noise from a sample from the Gaussian noise input $\mathbf{x}_T \sim \mathcal{N}(\mathbf{0}, \mathbf{I})$
 127 to gradually generate high-fidelity images. However, since the real reverse conditional distribution
 128 $q(x_{t-1} \mid x_t)$ is unavailable, diffusion models sample from a learned conditional distribution:

$$129 \quad p_\theta(\mathbf{x}_{t-1} \mid \mathbf{x}_t) = \mathcal{N}(\mathbf{x}_{t-1}; \mu_\theta(\mathbf{x}_t, t), \Sigma_\theta(\mathbf{x}_t, t)) \quad (2)$$

131 where $p(\mathbf{x}_T) \sim \mathcal{N}(\mathbf{x}_T; \mathbf{0}, \mathbf{I})$, with $\mu_\theta(\mathbf{x}_t, t)$ denotes the noise estimation model, and $\Sigma_\theta(\mathbf{x}_t, t)$ de-
 132 notes the variance for sampling which can be fixed to constants (Luo, 2022). The denoising process,
 133 constrained by the Markov chain, requires a huge number of iterative time steps in DDPM. DDIM
 134 generalizes the diffusion process to non-Markovian processes, simulating the diffusion process with
 135 fewer steps. It has replaced DDPM as the mainstream inference strategy. Our work focuses on
 136 accelerating the inference of the noise estimation model in DDIM, with a training-free PTQ process.

138 2.2 POST-TRAINING QUANTIZATION

139 The noise estimation models such as UNET (Podell et al., 2023) or Transformer (Chen et al., 2024;
 140 Yang et al., 2024; Zheng et al., 2024) exhibit high computational complexity, rendering the sam-
 141 pling of diffusion models computationally expensive. PTQ transforms the weights and activations
 142 of the full-precision model into a low-bit format, enabling the model’s inference process to utilize
 143 the integer matrix multiplication units on the target hardware platform and accelerating the compu-
 144 tational process (Jacob et al., 2018). Prior studies, such as PTQD (He et al., 2023) and Q-DM (Li
 145 et al., 2023b), have explored the application of quantization techniques for diffusion models. Q-
 146 Diffusion (Li et al., 2023a) and PTQ4DM (Shang et al., 2023) first achieved 8-bit quantization in
 147 text-to-image generation tasks. Subsequent research refined these methodologies through strategies
 148 such as sensitivity analysis (Yang et al., 2023) and timestep-aware quantization (Huang et al., 2024a;
 149 Wang et al., 2023). Among these works, MixDQ (Zhao et al., 2024b) introduces metric-decoupled
 150 sensitivity analysis and develops an integer programming-based method to derive optimal mixed-
 151 precision configurations. Qua2SeDiMo (Mills et al., 2025) enables high-quality mixed-precision
 152 quantization decisions for a wide range of diffusion models, from foundational U-Nets to state-of-
 153 the-art Transformers, extending the quantization lower bounds for image generation tasks to W4A8.
 154 SVDQuant (Li et al., 2024b) enhances quantization performance by integrating fine-grained quan-
 155 tization with singular value decomposition (SVD)-based weight decomposition, achieving W4A4
 156 quantization while maintaining acceptable quality degradation. Meanwhile, ViDiT-Q (Zhao et al.,
 157 2024a) further explores quantization for video generation tasks (Yang et al., 2024; Zheng et al.,
 158 2024), achieving W8A8 and W4A8 with negligible degradation in visual quality and metrics. These
 159 works minimize per-step errors through more precise quantization approximations at the layer level,
 160 yet overlook the error propagation in the diffusion process. Particularly in video generation tasks,
 161 which require a greater number of inference steps, the issue of error propagation becomes exacer-
 162 bated, and accumulated errors across sequential denoising stages fundamentally constrain the feasi-
 163 bility of lower-bit quantization. [Although several studies \(Chu et al., 2024; Yao et al., 2024\) have](#)

162
163

FP16

GGUF W4

ViDiT-Q W4A4

SVDQuant W4A4

TCEC W4A4



Figure 2: Qualitative visual results comparison. **Prompt1:** *An alien octopus floats through a portal reading a newspaper.* **Prompt2:** *A middle-aged woman of Asian descent, her dark hair streaked with silver, appears fractured and splintered, intricately embedded within a sea of broken porcelain. The porcelain glistens with splatter paint patterns in a harmonious blend of glossy and matte blues, greens, oranges, and reds, capturing her dance in a surreal juxtaposition of movement and stillness. Her skin tone, a light hue like the porcelain, adds an almost mystical quality to her form.*

recognized the issue of error propagation and attempted to propose solutions, their efforts are focused on "single-step error source suppression" (e.g., TAC decomposes input/noise errors, while QNCD targets noise in the embedding layer). These works neither elucidate the relationship between single-step errors and cumulative errors nor validate the model performance beyond small academic datasets such as CIFAR10.

Unlike prior studies, our method TCEC focuses on the error propagation problem in quantized diffusion models. We develop a theoretical framework that, through rigorous analysis, first models the relationship between per-step quantization errors and cumulative errors, derives a closed-form solution for cumulative errors, and then provides strategies to dynamically mitigate error accumulation during each denoising step.

3 METHOD

In this section, we first formally formulate the error propagation dynamics in quantized diffusion models and develop a preliminary analytical solution. Next, we establish theoretically-grounded approximations to reduce the computational complexity associated with cumulative error tracking. Finally, we propose a timestep-aware online estimation framework for per-step quantization errors, culminating in the TCEC mechanism - an efficient solution for real-time cumulative error mitigation.

3.1 ERROR PROPAGATION MECHANISMS

The iterative denoising process of diffusion models corresponds to the discrete approximation of the probability flow ordinary differential equation(PF-ODE), the noise at each time step $t \in [T, \dots, 1]$ is computed from x_t by a full-precision noise estimation model μ_θ whose weights are fixed at all steps. Based on DDIM-solver, we can calculate the sample x_{t-1} at time $t-1$ as follows:

$$x_{t-1} = \frac{\sqrt{\alpha_{t-1}}}{\sqrt{\alpha_t}} x_t + \left(\sqrt{1 - \alpha_{t-1}} - \frac{\sqrt{\alpha_{t-1}(1 - \alpha_t)}}{\sqrt{\alpha_t}} \right) \mu_\theta(x_t, t) \quad (3)$$

where α_t is a constant related to the noise schedule β_t and the specific relationship is $\frac{\alpha_t}{\alpha_{t-1}} = 1 - \beta_t$. Since $\beta_t \in (0, 1)$, α_t is monotonically decreasing with respect to t . We denote the quantized version

216 of the noise estimation model as $\tilde{\mu}_\theta$. When the input remains unchanged, it is formulated by:
 217

$$\tilde{\mu}_\theta(\tilde{\mathbf{x}}_t, t) = \mu_\theta(\tilde{\mathbf{x}}_t, t) + \varepsilon_t \quad (4)$$

219 where ε_t means per-step quantization error which is introduced due to model quantization and only
 220 relies on the module at iteration t and is independent of the others. The amount of error accumulated
 221 by continuously running the first $T - t + 1$ denoising steps is called the cumulative error δ_t , then
 222 the input including cumulative error can be expressed as $\tilde{x}_t = x_t + \delta_t$. Consequently, referring to
 223 Eq. 3, the iterative process of the quantized model can be expressed as:

$$\tilde{x}_{t-1} = \frac{\sqrt{\alpha_{t-1}}}{\sqrt{\alpha_t}} \tilde{x}_t + \left(\sqrt{1 - \alpha_{t-1}} - \frac{\sqrt{\alpha_{t-1}(1 - \alpha_t)}}{\sqrt{\alpha_t}} \right) \tilde{\mu}_\theta(\tilde{x}_t, t) \quad (5)$$

227 Based on Eq. 4 and the definition of cumulative error, Eq. 5 can be reformulated as:
 228

$$x_{t-1} + \delta_{t-1} = \frac{\sqrt{\alpha_{t-1}}}{\sqrt{\alpha_t}} (x_t + \delta_t) + \left(\sqrt{1 - \alpha_{t-1}} - \frac{\sqrt{\alpha_{t-1}(1 - \alpha_t)}}{\sqrt{\alpha_t}} \right) (\mu_\theta(x_t + \delta_t, t) + \varepsilon_t) \quad (6)$$

229 Applying the first-order Taylor expansion, $\mu_\theta(x_t + \delta_t, t)$ is approximated as $\mu_\theta(x_t, t) + \mathbf{J}_{x_t} \delta_t$.
 230 Substituting it into Eq. 6, we can obtain the error propagation equation that relates the per-step
 231 quantization error to the cumulative error:

$$\delta_{t-1} = A_t \delta_t + B_t \varepsilon_t \quad (7)$$

232 in which $A_t = \frac{\sqrt{\alpha_{t-1}}}{\sqrt{\alpha_t}} I + B_t * \mathbf{J}_{x_t}$, $B_t = \sqrt{1 - \alpha_{t-1}} - \frac{\sqrt{\alpha_{t-1}(1 - \alpha_t)}}{\sqrt{\alpha_t}}$ and $\mathbf{J}_{x_t} = \nabla_{x_t} \mu_\theta(x_t, t)$ is the
 233 Jacobian matrix of the denoising model μ_θ . Given that $\delta_T = 0$, when we recursively expand Eq. 7
 234 from T to t , the cumulative error δ_t can be derived as:

$$\delta_t = \sum_{k=t}^T \left(\prod_{j=t}^{k-1} A_j^{-1} \right) B_k \varepsilon_k \quad (8)$$

235 With this equation, we obtain a closed-form solution for the cumulative error corresponding to step t .
 236 By directly adding a correction term of $\Delta_t = -\delta_t$ to Eq. 3, the error introduced by quantization can
 237 be rectified. However, there are two issues in directly calculating Eq. 8: **Issue 1**—the existence of
 238 superimposed continuous multiplication and addition and the second derivative of the matrix makes
 239 the computational complexity unacceptable, and **Issue 2**—there is no explicit analytical solution for
 240 the per-step quantization error.

250 3.2 SIMPLIFY COMPUTATIONAL COMPLEXITY

251 In this section, we tackle **Issue 1** via reasonable approximation, thus simplifying the computational
 252 complexity of Δ_t .

253 **Approximation 1** For a well-trained diffusion model, it is insensitive to local changes in the input,
 254 which implies that we can ignore the Jacobian term: $\mathbf{J}_{x_t} \approx 0$. See Appendix B for details.

255 Consequently, the inverse of the propagation matrix \mathbf{A}_j can be approximately represented as
 256 $\frac{\sqrt{\alpha_j}}{\sqrt{\alpha_{j-1}}} \mathbf{I}$. By expanding the product terms in Eq. 8 and reducing the intermediate terms, the final
 257 result can be expressed as:

$$\prod_{j=t}^{k-1} A_j^{-1} = \prod_{j=t}^{k-1} \frac{\sqrt{\alpha_j}}{\sqrt{\alpha_{j-1}}} = \frac{\sqrt{\alpha_t}}{\sqrt{\alpha_{t-1}}} \cdot \frac{\sqrt{\alpha_{t+1}}}{\sqrt{\alpha_t}} \cdots = \frac{\sqrt{\alpha_{k-1}}}{\sqrt{\alpha_{t-1}}} \quad (9)$$

258 Plugging Eq. 9 into Eq. 8, we have:

$$\Delta_t = - \sum_{k=t}^T \left(\frac{\sqrt{\alpha_{k-1}}}{\sqrt{\alpha_{t-1}}} \right) B_k \varepsilon_k \quad (10)$$

259 Although the solution form has been greatly simplified, there are still difficulties, such as high
 260 computational complexity from time step T to t . To further speed up computation, we introduce an
 261 additional approximation, whose rationality will be rigorously proven later.

270 **Approximation 2** The correction term only takes into account the subsequent m steps. Since the
 271 denoising process unfolds in reverse, proceeding from T to 0, at the t -th step, only the quantization
 272 noises at steps $t + m, t + m - 1, \dots, t + 1$ are factored in. We refer to this as the temporal locality
 273 approximation.

274 Therefore, we can effectively reformulate Eq. 10 as:

$$276 \quad \Delta_t \approx -\frac{1}{\sqrt{\alpha_{t-1}}} \sum_{k=t}^{\min(t+m,T)} \sqrt{\alpha_{k-1}} \mathbf{B}_k \varepsilon_k \quad (11)$$

279 **How to determine the value of the parameter m ?** Based on our discussion in Sec. 3.1, the cumulative
 280 error at step $t - 1$ is related to the cumulative error δ_t from steps $[T, \dots, t + 1]$ and the per-step
 281 quantization error ε_t at step t . By substituting the correction term Δ_t into Eq. 7, we have:

$$283 \quad \widehat{\delta_{t-1}} = \mathbf{A}_t \delta_t + \mathbf{B}_t \varepsilon_t + \Delta_t \quad (12)$$

$$284 \quad = A_t \delta_t - \frac{1}{\sqrt{\alpha_{t-1}}} \sum_{k=t+1}^{\min(t+m,T)} \sqrt{\alpha_{k-1}} B_k \varepsilon_k$$

288 where $\widehat{\delta_{t-1}}$ is the corrected cumulative error and it should exhibits a strictly smaller upper bound in
 289 norm compared to δ_{t-1} , signifying a more refined and accurate error representation. Based on this,
 290 we can solve for the reasonable value of m . Under mild regularity conditions, there exists $\sigma > 0$
 291 independent of the timestep k , such that the per-step quantization error satisfies $\|\varepsilon_k\| \leq \sigma, \forall k$. Based
 292 on this condition, we can deduce from $\|\widehat{\delta_0}\| \leq \sigma \sum_{t=1}^T \left(\prod_{k=1}^{t-1} \rho_k \right) \|\mathbf{B}_t\| \leq \|\delta_0\|$ that $m = 1$. We
 293 provide a complete proof to this theorem in Appendix C and an empirical study demonstration
 294 in Appendix D. This implies that the cumulative error at any timestep is only related to the per-
 295 step quantization errors of the two immediately preceding steps. Thus, the final cumulative error
 296 correction term can be reformulated as:

$$297 \quad \Delta_t \approx -\frac{1}{\sqrt{\alpha_{t-1}}} \sum_{k=t}^{\min(t+1,T)} \sqrt{\alpha_{k-1}} \mathbf{B}_k \varepsilon_k \quad (13)$$

3.3 TIMESTEP-AWARE COMPENSATION

301 In this section, we address **Issue 2** to derive the definitive form of the correction terms. By visualizing and analyzing the noise estimation of the full-precision model ($\mu_\theta(\tilde{x}_t, t)$), the noise estimation of the quantized model ($\tilde{\mu}_\theta(\tilde{x}_t, t)$), and the output distortion (ε_t) across different time steps in
 302 Appendix F, two critical empirical observations emerge: **Timestep-Dependent Error Characteristics**—the per-step quantization error ε_t exhibits significant variations across timesteps, with distinct
 303 spatial and magnitude patterns at different stages of the denoising process. **Output-Correlated**
 304 **Error Propagation**—a strong statistical correlation exists between ε_t and the quantized model’s
 305 outputs $\tilde{\mu}_\theta(\tilde{x}_t, t)$, particularly in high-frequency regions.

306 These findings motivate our core proposition: *The per-step quantization error ε_t can be partially
 307 reconstructed by adaptively scaling the quantized noise estimates $\tilde{\mu}_\theta(\tilde{x}_t, t)$ with channel-specific
 308 coefficients.* Formally, we define the per-step quantization error as:

$$314 \quad \varepsilon_t = \mathbf{K}_t \odot \tilde{\mu}_\theta(\tilde{x}_t, t) \quad (14)$$

315 where $\mathbf{K}_t \in \mathbb{R}^C$ denotes a timestep-conditioned channel-wise scaling matrix, and \odot represents
 316 element-wise multiplication. We now focus on finding a loss function L , by minimizing which, we
 317 can efficiently reconstruct $\mu_\theta(\tilde{x}_t, t), \forall t \in [0, T]$. We adopt the Mean Squared Error (MSE) as the
 318 loss function and introduce regularization terms to prevent overfitting :

$$319 \quad \mathcal{L}(\mathbf{K}) = \sum_{t=1}^T \sum_{i=1}^C \sum_{j=1}^H \sum_{k=1}^W [(1 - K_{t,i}) \tilde{\mu}_{t,i,j,k} - \mu_{t,i,j,k}]^2 \quad (15)$$

$$320 \quad + \lambda_1 \sum_{t=1}^T \sum_{i=1}^C K_{t,i}^2$$

324 where T is the total denoising timesteps, C is the number of noise estimation channels, $H \times W$
 325 represents the spatial dimensions of feature maps and λ_1 restricts the magnitude of these coefficients.
 326 The loss function $\mathcal{L}(\mathbf{K})$ is strictly convex with respect to K , when $\lambda_1 > 0$. To derive the optimal
 327 scaling coefficients, set the first derivative to zero:

$$329 \quad \frac{\partial \mathcal{L}}{\partial K_{t,i}} = -2 \sum_{j=1}^H \sum_{k=1}^W [(1 - K_{t,i}) \tilde{\mu}_{t,i,j,k} - \mu_{t,i,j,k}] \tilde{\mu}_{t,i,j,k} + 2\lambda_1 K_{t,i} = 0 \quad (16)$$

332 Rearranging the terms, we obtain:

$$334 \quad K_{t,i} = \frac{\sum_{j=1}^H \sum_{k=1}^W (\tilde{\mu}_{t,i,j,k}^2 - \mu_{t,i,j,k} \tilde{\mu}_{t,i,j,k})}{\sum_{j=1}^H \sum_{k=1}^W \tilde{\mu}_{t,i,j,k}^2 + \lambda_1} \quad (17)$$

337 To prevent division by zero and ensure a stable and efficient reconstruction of quantization errors
 338 while maintaining theoretical rigor, we add $\gamma = 10^{-8}$ to the denominator.

340 Based on the provided calibration data, We can cache the noise prediction outputs of the full-
 341 precision model and the quantized model, and then compute $K \in \mathbb{R}^{T \times C}$ offline, which is directly
 342 used for quantization errors reconstruction during inference. Different values of λ_1 correspond to
 343 different values of K . We offer two methods, grid search and empirical rule, to determine the
 344 optimal value and compare their advantages and disadvantages. According to the experiments in
 345 Appendix G, the latter is adopted, that means $\lambda_1 = 0.01 \times \frac{\text{mean}(\tilde{\mu}^2)}{\text{var}(\mu)}$. Substituting Eq. 14 into Eq. 13,
 346 we obtain the final form of the closed-form solution for cumulative error:

$$347 \quad \Delta_t \approx -\frac{1}{\sqrt{\alpha_{t-1}}} \sum_{k=t}^{\min(t+1, T)} \sqrt{\alpha_{k-1}} \mathbf{B}_k \mathbf{K}_k \tilde{\mu}_\theta(\tilde{x}_k, k) \quad (18)$$

351 Eq. 18 indicates that relying on the outputs of the two immediately preceding steps $(t+1, t)$ of
 352 the quantized diffusion model, one can achieve a rapid estimation of the cumulative error at the
 353 current step (t) . This estimation stems from strict theoretical derivations, with the extra cost entailing
 354 minimal computations and caching the output of step $(t+1)$, which usually involves feature maps
 355 in a compact latent space.

356 4 EXPERIMENTS

359 4.1 IMPLEMENTATION DETAILS

360 **Quantization Scheme.** SVDQuant (Li et al., 2024b) introduces an additional low-rank branch that
 361 can mitigate quantization challenges in both weights and activations, establishing itself as a new
 362 benchmark for PTQ algorithms. In this study, we build our quantization strategy upon it by integrating
 363 cumulative error correction mechanisms. This approach ensures that performance comparisons
 364 remain unaffected by operator-level quantization configurations. In the 8-bit configuration, our ap-
 365 proach employs per-token dynamic quantization for activations and per-channel weight quantization,
 366 complemented by a low-rank auxiliary branch with a rank of 16. For the 4-bit configuration, we ap-
 367 pply per-group symmetric quantization to both activations and weights, using a low-rank branch with
 368 rank 32 and setting the group size to 64. All nonlinear activation and normalization layers are not
 369 quantized, meanwhile the inputs of linear layers in adaptive normalization are kept in 16 bits. To
 370 comprehensively evaluate the effectiveness of TCEC, we conducted comparative experiments with
 371 recent SOTA quantization algorithms across diverse generation tasks.

372 **Image Generation Evaluation.** We benchmark TCEC using SDXL (Podell et al., 2023), SDXL-
 373 Turbo (Podell et al., 2023) and PixArt models (Chen et al., 2023; 2024) including both the UNet
 374 and DiT backbones. SDXL-Turbo uses the default configuration of 4 inference steps, while SDXL
 375 employs the DDIM sampler with 50 steps. Since PixArt utilizes the DPM++ solver, we adapted
 376 TCEC to this advanced high-order solver to demonstrate its compatibility across different solvers.
 377 The detailed validation process is presented in Appendix E. To precompute the channel-wise scaling
 378 matrices K and λ_1 mentioned in section 3.3, we randomly sampled 1,024 prompts from COCO

378
 379 Table 1: Quantization Performance Comparison of Different Models. SDXL and SDXL-Turbo generate
 380 at 512^2 resolution, while PixArt achieves 1024^2 . Evaluation metrics include FID (distribution
 381 distance) (Parmar et al., 2024), IR (human preference) (Xu et al., 2023), LPIPS (perceptual similarity)
 382 (Zhang et al., 2018), and PSNR (numerical fidelity against 16-bit references) (Li et al., 2024b).

383 Model	384 Precision	385 Method	386 MJHQ				387 sDCI			
			388 FID↓	389 IR↑	390 LPIPS↓	391 PSNR↑	392 FID↓	393 IR↑	394 LPIPS↓	395 PSNR↑
386 SDXL	387 FP16	388 -	389 16.6	390 0.729	391 -	392 -	393 22.5	394 0.573	395 -	396 -
	387 W8A8	388 TensorRT	389 20.2	390 0.591	391 0.247	392 22.0	393 25.4	394 0.453	395 0.265	396 21.7
	387 W8A8	388 SVDQuant	389 16.6	390 0.718	391 0.119	392 26.4	393 22.4	394 0.574	395 0.129	396 25.9
	387 W8A8	388 SVDQuant + TCEC	389 16.0	390 0.728	391 0.092	392 27.3	393 22.0	394 0.580	395 0.103	396 26.7
	387 W4A4	388 SVDQuant	389 20.6	390 0.601	391 0.288	392 21.0	393 26.3	394 0.477	395 0.307	396 20.7
	387 W4A4	388 SVDQuant + TCEC	389 18.1	390 0.652	391 0.249	392 21.9	393 23.4	394 0.513	395 0.259	396 21.9
386 SDXL-Turbo	387 FP16	388 -	389 24.3	390 0.845	391 -	392 -	393 24.7	394 0.705	395 -	396 -
	387 W8A8	388 MixDQ	389 24.1	390 0.834	391 0.147	392 21.7	393 25.0	394 0.690	395 0.157	396 21.6
	387 W8A8	388 SVDQuant	389 24.3	390 0.845	391 0.100	392 24.0	393 24.8	394 0.701	395 0.110	396 23.7
	387 W8A8	388 SVDQuant + TCEC	389 24.5	390 0.849	391 0.083	392 24.9	393 23.9	394 0.720	395 0.098	396 24.5
	387 W4A4	388 MixDQ	389 27.7	390 0.708	391 0.402	392 15.7	393 25.9	394 0.610	395 0.415	396 15.7
	387 W4A4	388 MixDQ	389 353	390 -2.26	391 0.685	392 11.0	393 373	394 -2.28	395 0.686	396 11.3
386 PixArt- \sum	387 W4A4	388 SVDQuant	389 24.6	390 0.816	391 0.262	392 18.1	393 26.0	394 0.671	395 0.272	396 18.0
	387 W4A4	388 SVDQuant + TCEC	389 23.9	390 0.833	391 0.230	392 19.0	393 25.1	394 0.691	395 0.232	396 19.3
	387 FP16	388 -	389 16.6	390 0.944	391 -	392 -	393 24.8	394 0.966	395 -	396 -
	387 W8A8	388 ViDiT-Q	389 15.7	390 0.944	391 0.137	392 22.5	393 23.5	394 0.974	395 0.163	396 20.4
	387 W8A8	388 SVDQuant	389 16.3	390 0.955	391 0.109	392 23.7	393 24.2	394 0.969	395 0.129	396 21.8
	387 W8A8	388 SVDQuant + TCEC	389 16.2	390 0.964	391 0.098	392 24.5	393 23.4	394 0.952	395 0.118	396 22.6
401	402 W4A4	403 ViDiT-Q	404 412	405 -2.27	406 0.854	407 6.44	408 425	409 -2.28	410 0.838	411 6.70
	402 W4A4	403 SVDQuant	404 19.2	405 0.878	406 0.323	407 17.6	408 25.9	409 0.918	410 0.352	411 16.5
	402 W4A4	403 SVDQuant + TCEC	404 18.1	405 0.903	406 0.285	407 18.3	408 25.3	409 0.934	410 0.304	411 16.9

402 dataset (Chen et al., 2015) as the calibration dataset. [Appendix K provides a detailed explanation](#)
 403 of the selection and size of the calibration dataset. To evaluate the generalization capability of
 404 TCEC, we sample 5K prompts from the MJHQ-30K (Li et al., 2024a) and the summarized Densely
 405 Captioned Images(sDCI) (Urbanek et al., 2024) for benchmarking.

406 **Video Generation Evaluation.** We apply TCEC to OpenSORA (Zheng et al., 2024), the videos
 407 are generated with 100-steps DDIM with CFG scale of 4.0. We evaluate the quantized model on
 408 VBench (Huang et al., 2024b) to provide comprehensive results. Following prior research (Ren
 409 et al., 2024), we evaluate video quality from three distinct dimensions using eight carefully selected
 410 metrics. *Aesthetic Quality* and *Imaging Quality* focus on assessing the quality of individual frames,
 411 independent of temporal factors. *Subject Consistency*, *Background Consistency*, *Motion Smoothness*,
 412 and *Dynamic Degree* measure cross-frame temporal coherence and dynamics. Finally, *Scene Consistency*
 413 and *Overall Consistency* gauge the alignment of the video with the user-provided text
 414 prompt. We collected 128 samples from WebVid (Nan et al., 2024) as the calibration dataset to
 415 calculate K and λ_1 .

416 4.2 MAIN RESULTS

417 **Image Generation Evaluation.** As shown in Table 1, we conduct extensive experiments at two
 418 quantization precisions: W8A8 and W4A4. We observe that, across all precision levels, TCEC
 419 achieves better image fidelity and diversity, and it even matches the 16-bit results under W8A8 quantization.
 420 For UNet-based models, on SDXL, our W4A4 model substantially outperforms SVDQuant
 421 W4A4, the current SOTA 4-bit approach, achieving an sDCI PSNR of 21.9. This even surpasses TensorRT’s W8A8 result of 21.7, demonstrating robust performance under lower-bit quantization. On
 422 SDXL-Turbo, MixDQ W4A4 exhibits abnormal FID and IR metrics, indicating quantization failure.
 423 This highlights the greater difficulty of quantizing models with a small number of inference steps.
 424 Our W4A4 model surpasses SVDQuant by 0.017 and 0.02 in MJHQ IR and sDCI IR metrics, respec-
 425 tively, suggesting a stronger alignment with human preferences. [The larger performance gains of](#)
 426 [TCEC on SDXL compared to SDXL-Turbo highlight the critical role of cumulative error correction](#)
 427 [in longer inference sequences, and we provide a complete exploration of the minimal inference steps](#)
 428 [required for high-speed inference in Appendix H.](#) For DiT-based model, on PixArt- \sum , our W4A4
 429 model significantly surpasses SVDQuant’s W4A4 results across all metrics. Leveraging the DPM++
 430 solver, PixArt- \sum demonstrates TCEC’s robustness across different solver configurations. As shown

432
 433 Table 2: Performance of PTQ Algorithms for OpenSora on Vbench eval Benchmark. In the W4A8
 434 configuration, TCEC outperforms other methods.

Method	Bit-width W/A	Imaging Quality	Aesthetic Quality	Motion Smooth.	Dynamic Degree	BG. Consist.	Subject Consist.	Scene Consist.	Overall Consist.
-	16/16	63.68	57.12	96.28	56.94	96.13	90.28	39.61	26.21
Q-Diffusion	8/8	60.38	55.15	94.44	68.05	94.17	87.74	36.62	25.66
Q-DiT	8/8	60.35	55.80	93.64	68.05	94.70	86.94	32.34	26.09
PTQ4DiT	8/8	56.88	55.53	95.89	63.88	96.02	91.26	34.52	25.32
SmoothQuant	8/8	62.22	55.90	95.96	68.05	94.17	87.71	36.66	25.66
Quarot	8/8	60.14	53.21	94.98	66.21	95.03	85.35	35.65	25.43
ViDiT-Q	8/8	63.48	56.95	96.14	61.11	95.84	90.24	38.22	26.06
ViDiT-Q + TCEC	8/8	65.56	57.12	96.27	61.09	96.23	91.34	39.58	26.20
Q-DiT	4/8	23.30	29.61	97.89	4.166	97.02	91.51	0.00	4.985
PTQ4DiT	4/8	37.97	31.15	92.56	9.722	98.18	93.59	3.561	11.46
SmoothQuant	4/8	46.98	44.38	94.59	21.67	94.36	82.79	26.41	18.25
Quarot	4/8	44.25	43.78	92.57	66.21	94.25	84.55	28.43	18.43
ViDiT-Q	4/8	61.07	55.37	95.69	58.33	95.23	88.72	36.19	25.94
ViDiT-Q + TCEC	4/8	64.97	56.90	96.01	59.42	97.01	90.05	37.20	26.20

448
 449 in Figure 2, when compared with ViDiT-Q W4A4 and SVDQuant W4A4, the TECE W4A4 method
 450 demonstrates less quality degradation and smaller changes in image content. More visual results can
 451 be found in Appendix J.

452 **Video Generation Evaluation.** As shown in Table 2, our evaluation compares SOTA PTQ methods
 453 under both W8A8 and W4A8 configurations. In Imaging Quality, TCEC achieves 65.56 (W8A8)
 454 and 64.97 (W4A8), surpassing ViDiT-Q by +2.08 and +3.90 absolute points respectively. It demon-
 455 strates significant advantages in frame-wise quality metrics that evaluate static visual fidelity inde-
 456 pendent of temporal factors. TCEC achieves 96.27 motion smoothness at 8-bit and 96.01 at 4-bit
 457 quantization, outperforming ViDiT-Q by 0.13 and 0.32 respectively. This validates the effectiveness
 458 of our temporal-channel decoupled compensation strategy in handling error accumulation across
 459 denoising steps. The scene consistency metric reaches 39.58 (8-bit) and 37.20 (4-bit), establish-
 460 ing 1.36 and 1.01 improvements over baselines, which confirms stable long-sequence generation
 461 through temporal error propagation modeling.

462 **Hardware Resource Savings.** TCEC constructs its quantization strategy based on SVDQuant by in-
 463 tegrating cumulative error correction mechanisms. As TCEC’s research focus is not on engineering
 464 performance, we fully reuse its inference engine, Nunchaku (Li et al., 2024b). As shown in Table 3,
 465 experimental tests indicate that the resulting end-to-end (E2E) latency degradation is less than 0.5%.
 466 Further analysis can be found in the Appendix I. Therefore, on one 12B model, TCEC-W4A4 re-
 467 duces the memory footprint by $3.5 \times$ compared to the FP16 model and accelerates inference by $3 \times$
 468 versus NF4 weight-only quantization on the laptop-level RTX 4090, with engineering performance
 469 comparable to SVDQuant and significantly outperforming other PTQ algorithms.

471 Table 3: A comparison of inference overhead between ViDiT-Q and ViDiT-Q with TCEC.

Model	FP16	ViDiT-Q W8A8	ViDiT-Q+TCEC W8A8
Opensora1.2 (51 frames, 480P)	44.56 s	26.211s	26.316s
CogVideoX (48 frames, 480P)	78.48s	49.67s	49.894s
Wan2.1-1.3B (81 frames, 480P)	199 s	118.45s	119.029s

479 5 CONCLUSION

481 In this paper, we propose TCEC, a novel cumulative error correction strategy for quantized diffusion
 482 models. It develops a theoretical framework to effectively model the correlation between single-
 483 step quantization errors and cumulative errors, constructs error propagation equations for multi-
 484 ple solvers, and for the first time provides a closed-form solution for cumulative errors. Through
 485 timestep-aware online estimation of single-step quantization errors, TCEC enables low-cost and
 rapid correction of cumulative errors, with end-to-end latency degradation $\leq 0.5\%$. Experimental

486 results show that TCEC achieves the SOTA quantization performance under the W4A4 configura-
 487 tion while maintaining orthogonality to existing PTQ algorithms that minimize per-step quantization
 488 errors.
 489

490 6 ETHICS STATEMENT 491

492 This work complies with the ICLR Code of Ethics. No human subjects or animal experimentation
 493 were involved in this study. All datasets used, were obtained in accordance with relevant usage
 494 policies, ensuring that privacy was not violated. We have taken care to mitigate potential biases
 495 and to prevent discriminatory outcomes in our research. No personally identifiable information was
 496 utilized, and no experiments were conducted that might raise privacy or security concerns. We are
 497 committed to upholding transparency and integrity throughout the entirety of this research.
 498

499 7 REPRODUCIBILITY STATEMENT 500

501 We have made every effort to ensure that the results presented in this paper are reproducible. The ex-
 502 perimental setup, including training steps, model configurations, and hardware details, is described
 503 in detail in the paper. We have also provided a full description of our proposed TCEC strategy, to
 504 assist others in reproducing our experiments. Additionally, we evaluate our method against recent
 505 state-of-the-art PTQ algorithms across diverse generation tasks, using publicly available datasets.
 506 These datasets are openly accessible, ensuring consistent and reproducible evaluation results.
 507

508 We believe these measures will enable other researchers to reproduce our work and further advance
 509 the field.
 510

511 REFERENCES

512 Yash Bhalgat, Jinwon Lee, Markus Nagel, Tijmen Blankevoort, and Nojun Kwak. Lsq+: Improving
 513 low-bit quantization through learnable offsets and better initialization. In *Proceedings of the*
 514 *IEEE/CVF conference on computer vision and pattern recognition workshops*, pp. 696–697, 2020.

515 Yaohui Cai, Zhewei Yao, Zhen Dong, Amir Gholami, Michael W Mahoney, and Kurt Keutzer.
 516 Zeroq: A novel zero shot quantization framework. In *Proceedings of the IEEE/CVF conference*
 517 *on computer vision and pattern recognition*, pp. 13169–13178, 2020.

518 Junsong Chen, Jincheng Yu, Chongjian Ge, Lewei Yao, Enze Xie, Yue Wu, Zhongdao Wang, James
 519 Kwok, Ping Luo, Huchuan Lu, et al. Pixart- α : Fast training of diffusion transformer for photore-
 520 alistic text-to-image synthesis. *arXiv preprint arXiv:2310.00426*, 2023.

521 Junsong Chen, Chongjian Ge, Enze Xie, Yue Wu, Lewei Yao, Xiaozhe Ren, Zhongdao Wang, Ping
 522 Luo, Huchuan Lu, and Zhenguo Li. Pixart- σ : Weak-to-strong training of diffusion transformer for
 523 4k text-to-image generation. In *European Conference on Computer Vision*, pp. 74–91. Springer,
 524 2024.

525 Xinlei Chen, Hao Fang, Tsung-Yi Lin, Ramakrishna Vedantam, Saurabh Gupta, Piotr Dollár, and
 526 C Lawrence Zitnick. Microsoft coco captions: Data collection and evaluation server. *arXiv*
 527 *preprint arXiv:1504.00325*, 2015.

528 Huanpeng Chu, Wei Wu, Chengjie Zang, and Kun Yuan. Qncd: Quantization noise correction for
 529 diffusion models. In *Proceedings of the 32nd ACM International Conference on Multimedia*, pp.
 530 10995–11003, 2024.

531 Yefei He, Luping Liu, Jing Liu, Weijia Wu, Hong Zhou, and Bohan Zhuang. Ptqd: Accurate post-
 532 training quantization for diffusion models. *arXiv preprint arXiv:2305.10657*, 2023.

533 Jonathan Ho, Ajay Jain, and Pieter Abbeel. Denoising diffusion probabilistic models. *Advances in*
 534 *neural information processing systems*, 33:6840–6851, 2020.

535 Yushi Huang, Ruihao Gong, Jing Liu, Tianlong Chen, and Xianglong Liu. Tfmq-dm: Temporal fea-
 536 ture maintenance quantization for diffusion models. In *Proceedings of the IEEE/CVF Conference*
 537 *on Computer Vision and Pattern Recognition*, pp. 7362–7371, 2024a.

540 Ziqi Huang, Yinan He, Jiashuo Yu, Fan Zhang, Chenyang Si, Yuming Jiang, Yuanhan Zhang, Tianx-
 541 ing Wu, Qingyang Jin, Nattapol Chanpaisit, et al. Vbench: Comprehensive benchmark suite for
 542 video generative models. In *Proceedings of the IEEE/CVF Conference on Computer Vision and*
 543 *Pattern Recognition*, pp. 21807–21818, 2024b.

544 Benoit Jacob, Skirmantas Kligys, Bo Chen, Menglong Zhu, Matthew Tang, Andrew Howard,
 545 Hartwig Adam, and Dmitry Kalenichenko. Quantization and training of neural networks for
 546 efficient integer-arithmetic-only inference. In *Proceedings of the IEEE conference on computer*
 547 *vision and pattern recognition*, pp. 2704–2713, 2018.

549 Daiqing Li, Aleks Kamko, Ehsan Akhgari, Ali Sabet, Linmiao Xu, and Suhail Doshi. Playground
 550 v2. 5: Three insights towards enhancing aesthetic quality in text-to-image generation. *arXiv*
 551 *preprint arXiv:2402.17245*, 2024a.

552 Muyang Li, Yujun Lin, Zhekai Zhang, Tianle Cai, Xiuyu Li, Junxian Guo, Enze Xie, Chenlin Meng,
 553 Jun-Yan Zhu, and Song Han. Svdqunat: Absorbing outliers by low-rank components for 4-bit
 554 diffusion models. *arXiv preprint arXiv:2411.05007*, 2024b.

556 Xiuyu Li, Yijiang Liu, Long Lian, Huanrui Yang, Zhen Dong, Daniel Kang, Shanghang Zhang,
 557 and Kurt Keutzer. Q-diffusion: Quantizing diffusion models. In *Proceedings of the IEEE/CVF*
 558 *International Conference on Computer Vision*, pp. 17535–17545, 2023a.

560 Yanjing Li, Sheng Xu, Xianbin Cao, Xiao Sun, and Baochang Zhang. Q-dm: An efficient low-bit
 561 quantized diffusion model. *Advances in neural information processing systems*, 36:76680–76691,
 562 2023b.

563 Cheng Lu, Yuhao Zhou, Fan Bao, Jianfei Chen, Chongxuan Li, and Jun Zhu. Dpm-solver: A fast
 564 ode solver for diffusion probabilistic model sampling in around 10 steps. *Advances in Neural*
 565 *Information Processing Systems*, 35:5775–5787, 2022.

567 Calvin Luo. Understanding diffusion models: A unified perspective. *arXiv preprint*
 568 *arXiv:2208.11970*, 2022.

569 Keith G Mills, Mohammad Salameh, Ruichen Chen, Negar Hassanzadeh, Wei Lu, and Di Niu.
 570 Qua2sedimo: Quantifiable quantization sensitivity of diffusion models. In *Proceedings of the*
 571 *AAAI Conference on Artificial Intelligence*, volume 39, pp. 6153–6163, 2025.

573 Kepan Nan, Rui Xie, Penghao Zhou, Tiehan Fan, Zhenheng Yang, Zhijie Chen, Xiang Li, Jian Yang,
 574 and Ying Tai. Openvid-1m: A large-scale high-quality dataset for text-to-video generation. *arXiv*
 575 *preprint arXiv:2407.02371*, 2024.

577 Gaurav Parmar, Taesung Park, Srinivasa Narasimhan, and Jun-Yan Zhu. One-step image translation
 578 with text-to-image models. *arXiv preprint arXiv:2403.12036*, 2024.

579 Dustin Podell, Zion English, Kyle Lacey, Andreas Blattmann, Tim Dockhorn, Jonas Müller, Joe
 580 Penna, and Robin Rombach. Sdxl: Improving latent diffusion models for high-resolution image
 581 synthesis. *arXiv preprint arXiv:2307.01952*, 2023.

583 Weiming Ren, Huan Yang, Ge Zhang, Cong Wei, Xinrun Du, Wenhao Huang, and Wenhui
 584 Chen. Consisti2v: Enhancing visual consistency for image-to-video generation. *arXiv preprint*
 585 *arXiv:2402.04324*, 2024.

586 Hiroshi Sasaki, Chris G Willcocks, and Toby P Breckon. Unit-ddpm: Unpaired image translation
 587 with denoising diffusion probabilistic models. *arXiv preprint arXiv:2104.05358*, 2021.

589 Yuzhang Shang, Zhihang Yuan, Bin Xie, Bingzhe Wu, and Yan Yan. Post-training quantization on
 590 diffusion models. In *Proceedings of the IEEE/CVF conference on computer vision and pattern*
 591 *recognition*, pp. 1972–1981, 2023.

592 Jiaming Song, Chenlin Meng, and Stefano Ermon. Denoising diffusion implicit models. *arXiv*
 593 *preprint arXiv:2010.02502*, 2020.

594 Jack Urbanek, Florian Bordes, Pietro Astolfi, Mary Williamson, Vasu Sharma, and Adriana Romero-
 595 Soriano. A picture is worth more than 77 text tokens: Evaluating clip-style models on dense cap-
 596 tions. In *Proceedings of the IEEE/CVF Conference on Computer Vision and Pattern Recognition*,
 597 pp. 26700–26709, 2024.

598 Changyuan Wang, Ziwei Wang, Xiuwei Xu, Yansong Tang, Jie Zhou, and Jiwen Lu. Towards
 599 accurate post-training quantization for diffusion models. *arXiv preprint arXiv:2305.18723*, 2023.

600 Di Wu, Qi Tang, Yongle Zhao, Ming Zhang, Ying Fu, and Debing Zhang. Easyquant: Post-training
 601 quantization via scale optimization. *arXiv preprint arXiv:2006.16669*, 2020.

602 Junyi Wu, Haoxuan Wang, Yuzhang Shang, Mubarak Shah, and Yan Yan. Ptq4dit: Post-training
 603 quantization for diffusion transformers. *arXiv preprint arXiv:2405.16005*, 2024.

604 Jiazheng Xu, Xiao Liu, Yuchen Wu, Yuxuan Tong, Qinkai Li, Ming Ding, Jie Tang, and Yuxiao
 605 Dong. Imagereward: Learning and evaluating human preferences for text-to-image generation.
 606 *Advances in Neural Information Processing Systems*, 36:15903–15935, 2023.

607 Yuewei Yang, Xiaoliang Dai, Jialiang Wang, Peizhao Zhang, and Hongbo Zhang. Efficient quanti-
 608 zation strategies for latent diffusion models. *arXiv preprint arXiv:2312.05431*, 2023.

609 Zhuoyi Yang, Jiayan Teng, Wendi Zheng, Ming Ding, Shiyu Huang, Jiazheng Xu, Yuanming Yang,
 610 Wenyi Hong, Xiaohan Zhang, Guanyu Feng, et al. Cogvideox: Text-to-video diffusion models
 611 with an expert transformer. *arXiv preprint arXiv:2408.06072*, 2024.

612 Yuzhe Yao, Feng Tian, Jun Chen, Haonan Lin, Guang Dai, Yong Liu, and Jingdong Wang. Timestep-
 613 aware correction for quantized diffusion models. In *European Conference on Computer Vision*,
 614 pp. 215–232. Springer, 2024.

615 Richard Zhang, Phillip Isola, Alexei A Efros, Eli Shechtman, and Oliver Wang. The unreasonable
 616 effectiveness of deep features as a perceptual metric. In *Proceedings of the IEEE conference on*
 617 *computer vision and pattern recognition*, pp. 586–595, 2018.

618 Tianchen Zhao, Tongcheng Fang, Haofeng Huang, Enshu Liu, Rui Wan, Widjadewi Soedarmadji,
 619 Shiyao Li, Zinan Lin, Guohao Dai, Shengen Yan, et al. Vudit-q: Efficient and accurate quantiza-
 620 tion of diffusion transformers for image and video generation. *arXiv preprint arXiv:2406.02540*,
 621 2024a.

622 Tianchen Zhao, Xuefei Ning, Tongcheng Fang, Enshu Liu, Guyue Huang, Zinan Lin, Shengen Yan,
 623 Guohao Dai, and Yu Wang. Mixdq: Memory-efficient few-step text-to-image diffusion mod-
 624 els with metric-decoupled mixed precision quantization. In *European Conference on Computer*
 625 *Vision*, pp. 285–302. Springer, 2024b.

626 Zangwei Zheng, Xiangyu Peng, Tianji Yang, Chenhui Shen, Shenggui Li, Hongxin Liu, Yukun
 627 Zhou, Tianyi Li, and Yang You. Open-sora: Democratizing efficient video production for all.
 628 *arXiv preprint arXiv:2412.20404*, 2024.

629

630

631

632

633

634

635

636

637

638

639

640

641

642

643

644

645

646

647

648

APPENDIX

649

650

651

A LLM USAGE

652

653

654

655

656

657

658

Large Language Models were used solely to refine the manuscript’s language, including sentence rephrasing, grammar checking, and improving readability. The LLM was not involved in ideation, methodology, experimental design, or data analysis. All scientific content, concepts, and analyses were developed by the authors, who take full responsibility for the manuscript. The LLM’s role was limited to linguistic polishing, with strict adherence to ethical guidelines and avoidance of plagiarism or scientific misconduct.

659

660

B EXPLANATION OF APPROXIMATION 1

661

662

In Approximation 1, we approximate $J_{x_t} \approx 0$. However, we clarify that this approximation does not ‘deny the existence of the Jacobian’. Rather, based on magnitude analysis of error propagation and the inherent properties of diffusion models, we argue that its contribution to cumulative error is negligible compared to the dominant terms. This makes the approximation a theoretically grounded and empirically supported simplification. The details are as follows:

1. Core rationale of the approximation: a magnitude-first simplification. In the error propagation equation (Eq. 7), the propagation matrix $A_t = \frac{\sqrt{\alpha_{t-1}}}{\sqrt{\alpha_t}} I + B_t \cdot J_{x_t}$ is composed of two components:

663

664

665

666

667

668

669

- **Dominant term $\frac{\sqrt{\alpha_{t-1}}}{\sqrt{\alpha_t}} I$** : This term arises from the diffusion noise-scheduling mechanism (where α_t is tied to the noise variance β_t). Its magnitude consistently falls in the 0.9–1.0 range, making it the primary driver of error propagation, typically contributing over 95% of the total effect.
- **Secondary term $B_t \cdot J_{x_t}$** : Here, B_t is an α_t -dependent coefficient with magnitude ≤ 0.05 . Meanwhile, for a well-trained diffusion model optimized via “denoising score matching,” the noise estimator μ_θ satisfies a Lipschitz continuity condition with constant $L < 0.3$, implying $\|J_{x_t}\| \leq L$. Consequently, the magnitude of $B_t \cdot J_{x_t}$ is at most 1/100–1/10 of the dominant term. Its influence on the distribution of accumulated error is therefore minimal.

670

2. Support from both theoretical insights and empirical evidence. From a theoretical standpoint, the intermediate states x_t in diffusion models are well known to approximate a standard Gaussian distribution at most timesteps due to strong noise injection. This heavy smoothing of the input space forces the model to focus primarily on global noise evolution rather than local perturbations, which naturally suppresses the influence of the Jacobian term J_{x_t} . From an empirical standpoint, as shown in Table 4 we measure the ratio between the secondary term and the dominant term across different timesteps using SDXL under W4A4 quantization. Even in low-noise regimes (e.g., timestep $t = 40$), the secondary term contributes only 0.45% relative to the dominant term—well within the threshold of being safely negligible in magnitude.

671

672

673

674

675

676

677

678

679

680

681

682

683

684

685

686

687

688

689

690

691

Table 4: Statistics of dominant and secondary terms at different SDXL timesteps.

time step (SDXL, T=50)	Dominant term	J_{x_t}	$B_t \cdot J_{x_t}$	Secondary / Dominant
10 (High-noise stage)	0.982	0.021	0.00105	0.107%
25 (Intermediate stage)	0.951	0.037	0.00185	0.194%
40 (Low-noise stage)	0.915	0.083	0.00415	0.454%

692

693

694

695

696

697

698

699

700

701

3. Necessity of the simplification. If the Jacobian term were retained, computing the full error propagation would require matrix inversion and higher-order derivatives, causing the computational complexity to surge from $\mathcal{O}(T)$ to $\mathcal{O}(T \cdot C^2 \cdot H \cdot W)$, which is infeasible for real-time online compensation. In contrast, the simplified formulation preserves the accuracy of accumulated-error estimation (with deviation $\pm 1\%$), while remaining practical for deployment in real systems.

702 C DERIVATION OF ERROR ACCUMULATION STEPS 703

704 In this section, we derive the reasonable value of the Error Accumulation Steps m by starting from
705 the principle that the correction term should reduce the norm upper bound of the cumulative error.
706

707 As described in Sec. 3.2, the cumulative error with the correction term added can be expressed as:
708

$$709 \widehat{\delta_{t-1}} = A_t \delta_t - \frac{1}{\sqrt{\alpha_{t-1}}} \sum_{k=t+1}^{\min(t+m,T)} \sqrt{\alpha_{k-1}} B_k \varepsilon_k \quad (19)$$

711 where $\widehat{\delta_{t-1}}$ is the corrected cumulative error and it should exhibits a strictly smaller upper bound in
712 norm compared to δ_{t-1} , signifying a more refined and accurate error representation.
713

714 Under mild regularity conditions, there exists $\sigma > 0$ independent of the timestep k , such that the
715 per-step quantization error satisfies $\|\varepsilon_k\| \leq \sigma, \forall k$. Analyze the upper bound of the norm of the
716 error-propagation coefficient matrix. The original propagation coefficient is:
717

$$718 \mathbf{A}_t = \frac{\sqrt{\alpha_{t-1}}}{\sqrt{\alpha_t}} \mathbf{I} + B_t * \mathbf{J}_{x_t} \quad (20)$$

720 For a model that has converged during training, there exists a constant L such that $\forall t, \|\mathbf{J}_t\| \leq L$.
721 Then we have:
722

$$723 |\mathbf{A}_t| \leq \frac{\sqrt{\alpha_{t-1}}}{\sqrt{\alpha_t}} + |\mathbf{B}_t|L \quad (21)$$

724 Based on the above-known conditions, since $\frac{\sqrt{\alpha_{t-1}}}{\sqrt{\alpha_t}}$ and $\|\mathbf{B}_t\|L$ are constants, there exists ρ_t such
725 that:
726

$$727 |\mathbf{A}_t| \leq \rho_t \quad (22)$$

728 Substitute it into the original error-propagation equation and solve for the upper bound of its norm.
729 We can know that the following equation holds:
730

$$731 \widehat{|\delta_{t-1}|} \leq \rho_t |\delta_t| + \frac{1}{\sqrt{\alpha_{t-1}}} \sum_{k=t+1}^{\min(t+m,T)} \sqrt{\alpha_{k-1}} |\mathbf{B}_k| \sigma \quad (23)$$

734 Define the corrected noise residue term as:
735

$$736 \eta_t = \frac{1}{\sqrt{\alpha_{t-1}}} \sum_{k=t+1}^{\min(t+m,T)} \sqrt{\alpha_{k-1}} |\mathbf{B}_k| \sigma \quad (24)$$

739 Then the upper bound of the error recursion can be expressed as:
740

$$741 \widehat{|\delta_{t-1}|} \leq \rho_t |\delta_t| + \eta_t \quad (25)$$

742 Next, we need to go from the time step $t = T$ to $t = 0$, and it is obvious that $\widehat{\delta_T} = 0$. At this time,
743 we can get:
744

$$745 |\widehat{\delta}_0| \leq \sum_{t=1}^T \left(\prod_{k=1}^{t-1} \rho_k \right) \eta_t \quad (26)$$

747 After substituting the noise residue term, we can obtain the upper bound of the norm of the error-
748 propagation equation with the correction term added:
749

$$750 |\widehat{\delta}_0| \leq \sigma \sum_{t=1}^T \left(\prod_{k=1}^{t-1} \rho_k \right) \frac{1}{\sqrt{\alpha_{t-1}}} \sum_{k=t+1}^{\min(t+m,T)} \sqrt{\alpha_{k-1}} |\mathbf{B}_k| \quad (27)$$

753 Since α_t is monotonically decreasing and $k \geq t + 1$, this means:
754

$$755 \frac{\sqrt{\alpha_{k-1}}}{\sqrt{\alpha_{t-1}}} \leq 1 \Rightarrow \sqrt{\alpha_{k-1}} \leq \sqrt{\alpha_{t-1}} \quad (28)$$

756 Then

$$\frac{1}{\sqrt{\alpha_{t-1}}} \sum_{k=t+1}^{\min(t+m,T)} \sqrt{\alpha_{k-1}} \|\mathbf{B}_k\| \leq \sum_{k=t+1}^{\min(t+m,T)} \|\mathbf{B}_k\| \quad (29)$$

760 Therefore, $\hat{\delta}_0$ satisfies the following relationship

$$|\hat{\delta}_0| \leq \sigma \sum_{t=1}^T \left(\prod_{k=1}^{t-1} \rho_k \right) \sum_{k=t+1}^{\min(t+m,T)} \|\mathbf{B}_k\| \quad (30)$$

765 The uncorrected error-propagation equation is

$$\delta_{t-1} = \mathbf{A}_t \delta_t + \mathbf{B}_t \varepsilon_t \quad (31)$$

768 By recursive expansion, we can calculate that the upper bound of its norm is

$$|\delta_0| \leq \sigma \sum_{t=1}^T \left(\prod_{k=1}^{t-1} \rho_k \right) |\mathbf{B}_t| \quad (32)$$

772 Combining Eq. 30 and Eq. 32, for $\hat{\delta}_0 < \delta_0$ to hold, it can be achieved by satisfying the following
773 relationship

$$\frac{1}{\sqrt{\alpha_{t-1}}} \sum_{k=t+1}^{\min(t+m,T)} \sqrt{\alpha_{k-1}} \|\mathbf{B}_k\| \leq \sum_{k=t+1}^{\min(t+m,T)} \|\mathbf{B}_k\| \quad (33)$$

777 Ultimately, the following formula needs to hold

$$\sum_{k=t+1}^{\min(t+m,T)} \|\mathbf{B}_k\| \leq \|\mathbf{B}_t\| \quad (34)$$

781 Obviously, the value of m should be 1. This implies that at time step t , only the quantization errors
782 at steps $t+1$ and t need to be considered.784

D EMPIRICAL STUDY OF ERROR ACCUMULATION STEPS

786 Starting from the proposed mathematical model, we derive the original form of the correction term
787 Eq. 10, so we can get the recursive formula $\Delta_t = \frac{\sqrt{\alpha_t}}{\sqrt{\alpha_{t-1}}} \Delta_{t-1} - B_t \varepsilon_t$. Then, based on the constraint
788 that "the error upper bound decreases after adding the correction term", we present the actual ap-
789 proximate solution Eq. 13, the recursive formula is $\Delta_t \approx \frac{\sqrt{\alpha_t}}{\sqrt{\alpha_{t-1}}} B_{t+1} \varepsilon_{t+1} - B_t \varepsilon_t$. [Appendix C](#) presents the complete derivation process. It is important to emphasize that the aforementioned
790 transformation involves no errors when $m = T - t$; in essence, it is merely a formal transformation
791 designed to facilitate subsequent analysis. On this basis, we conducted rigorous mathematical
792 derivation and proof for the selection of m , with the explicit objective of "reducing the error upper
793 bound after introducing the correction term δ_t ". Eventually, the optimal solution $m = 1$ was ob-
794 tained. This implies that at any time step, the cumulative error of the model is only related to the
795 step-wise quantization errors of the immediately preceding two time steps—a finding that constitutes
796 one of the core contributions of this study.799 As shown in Table 5, we further supplement the actual test data based on the SDXL and PixArt- σ
800 models with backbones quantized using SVDQuant. It is observed that the performance of iterative
801 solving based on Eq. 10 is significantly inferior to that of two-step approximate solving based on
802 Eq. 13.804

E COMPATIBILITY WITH DIFFERENT SOLVERS.

806 In this section, we extend TCEC to other solvers to demonstrate its generality, such as the most
807 commonly used high-order solver DPM++ (Lu et al., 2022). The iterative update for DPM-Solver++
808 (2nd-order variant) is given by:

$$x_{t-1} = x_t + \frac{\Delta t}{2} [f_\theta(x_t, t) + f_\theta(x_t + \Delta t \cdot f_\theta(x_t, t), t - \Delta t)] \quad (35)$$

Table 5: Quantization Performance Comparison of Different Models.

Model	Method	FID \downarrow	IR \uparrow	LPIPS \downarrow	PSNR \uparrow
SDXL	FP16	16.60	0.729	-	-
	SVDQuant	16.6	0.718	0.119	26.4
	TCEC (Eq. 10)	16.5	0.710	0.121	26.1
	TCEC (Eq. 13)	16.0	0.728	0.092	27.3
PixArt- σ	FP16	16.6	0.944	-	-
	SVDQuant	16.3	0.955	0.109	23.7
	TCEC (Eq. 10)	16.5	0.932	0.112	23.3
	TCEC (Eq. 13)	16.2	0.964	0.098	24.5

where $f_\theta(x, t) = -\frac{1}{\sqrt{1-\alpha_t}}\mu_\theta(x_t, t)$ represents the noise prediction network. Let $\tilde{f}_\theta = f_\theta + \varepsilon_t$ denote the quantized prediction, where ε_t is the per-step quantization error. The perturbed update becomes:

$$\tilde{x}_{t-1} = x_{t-1} + \delta_{t-1} = \Phi(\tilde{x}_t, \tilde{f}_\theta) \quad (36)$$

Expanding to second-order Taylor series:

$$\delta_{t-1} = \underbrace{\frac{\partial \Phi}{\partial x_t} \delta_t}_{\text{Linear Term}} + \underbrace{\frac{\partial \Phi}{\partial f_t} \varepsilon_t}_{\text{Quantization Error}} + \underbrace{\frac{1}{2} \frac{\partial^2 \Phi}{\partial x_t^2} \delta_t^2}_{\text{Nonlinear Term}} + \mathcal{O}(\delta_t^3) \quad (37)$$

Neglecting higher-order terms, define propagation matrices:

$$\mathbf{A}_t = \frac{\partial \Phi}{\partial x_t} = \mathbf{I} + \frac{\Delta t}{2} (\mathbf{J}_{f_t} + \mathbf{J}_{f_{t-\Delta t}} \cdot (\mathbf{I} + \Delta_t \mathbf{J}_{f_t})) \quad (38)$$

$$\mathbf{B}_t = \frac{\partial \Phi}{\partial f_t} = \frac{\Delta t}{2} [\mathbf{I} + (\mathbf{I} + \Delta_t \mathbf{J}_{f_t})] \quad (39)$$

where $\mathbf{J}_{f_t} = \nabla_x f_\theta(x_t, t)$ is the Jacobian matrix. Then, we can obtain the error propagation equation that relates the per-step quantization error to the cumulative error:

$$\delta_{t-1} = \mathbf{A}_t \delta_t + \mathbf{B}_t \varepsilon_t \quad (40)$$

DPM has an error-propagation equation structurally similar to that of DDIM, with only differences in propagation coefficients. This demonstrates the generality of our theoretical framework.

The error propagation incorporates temporal dependencies:

$$\delta_{t-1} = \prod_{k=t}^{t+m} \mathbf{A}_k \delta_{t+m} + \sum_{k=t}^{t+m} \left(\prod_{j=t}^{k-1} \mathbf{A}_j \right) \mathbf{B}_k \varepsilon_k \quad (41)$$

with window size $m = 2$ for 2nd-order DPM-Solver++. Implement truncated SVD for computational efficiency:

$$\mathbf{J}_{f_t} \approx \mathbf{U}_t \boldsymbol{\Sigma}_t \mathbf{V}_t^T \quad (\text{rank} \leq r) \quad (42)$$

Yielding approximated propagation:

$$\mathbf{A}_t \approx \mathbf{I} + \frac{\Delta t}{2} (\mathbf{U}_t \boldsymbol{\Sigma}_t \mathbf{V}_t^T + \mathbf{U}_{t-\Delta t} \boldsymbol{\Sigma}_{t-\Delta t} \mathbf{V}_{t-\Delta t}^T \cdot (\mathbf{I} + \Delta_t \mathbf{U}_t \boldsymbol{\Sigma}_t \mathbf{V}_t^T)) \quad (43)$$

The error correction term becomes:

$$\Delta_t^{\text{DPM++}} = - \sum_{k=t}^{t+2} \gamma_k \mathbf{B}_k \varepsilon_k \quad (44)$$

with temporal weights:

$$\gamma_k = \frac{\sqrt{\alpha_{k-1}}}{\sqrt{\alpha_{t-1}}} \cdot \exp \left(-\lambda \sum_{j=t}^k \|\mathbf{J}_{f_j}\|_F \right) \quad (45)$$

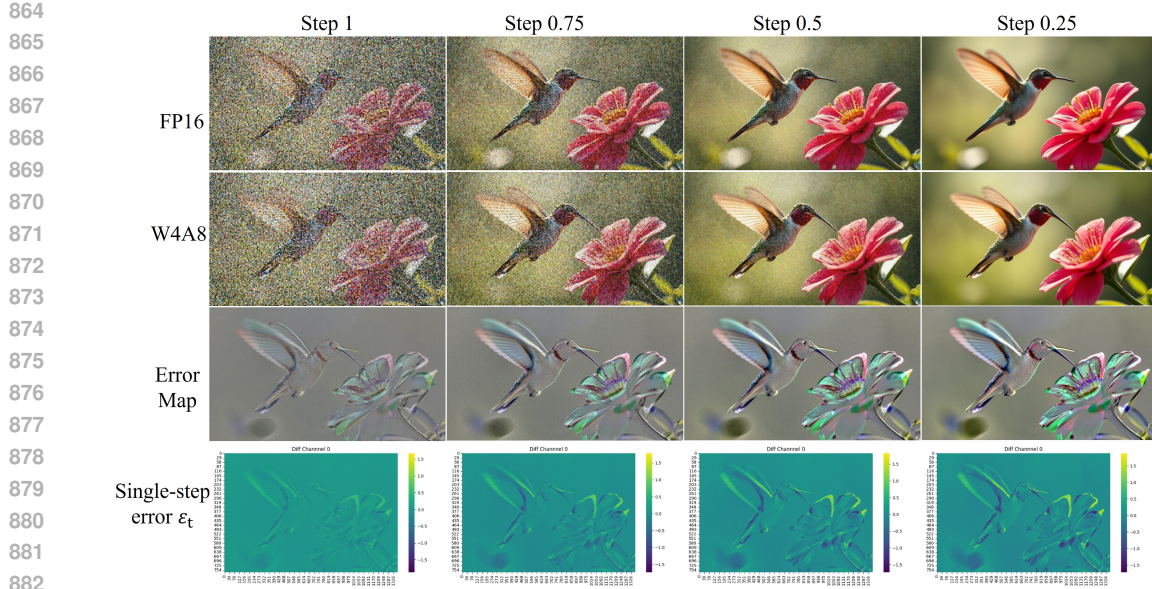


Figure 3: **Flux visualization of quantization errors during denoising.** We compare the full-precision model (FP16) and the quantized model (W4A8) under the prompt “hummingbird flying near a flower. 4k ultra realistic ray tracing dynamic lighting” with hyperparameters `num_timesteps=4` and `guidance_scale=3.5`. The figure illustrates three key phenomena: (1) quantization errors accumulate as denoising progresses ($\text{Step 1} \rightarrow 0.75 \rightarrow 0.5 \rightarrow 0.25$), exhibiting distinct spatial structures; (2) the errors are strongly correlated with the model outputs, particularly along object boundaries and textured regions; and (3) high-frequency components such as feather edges and flower petals amplify the discrepancies, highlighting the **timestep-dependent** and **output-correlated** nature of error propagation in quantized diffusion models.

F TIMESTEP-AWARE QUANTIZATION ERROR

As illustrated in the Figure 3, we compare the generation results of the full-precision model (FP16) and the quantized model (W4A8) across different denoising steps. Three key empirical observations emerge:

- **Cumulative evolution of errors:** At early steps (e.g., Step 1), the discrepancy between FP16 and W4A8 is relatively small, but the error gradually accumulates as denoising proceeds ($\text{Step 0.75} \rightarrow 0.5 \rightarrow 0.25$), exhibiting distinct spatial structures. This corroborates our finding of Timestep-Dependent Error Characteristics, indicating that quantization error is not uniformly distributed but evolves dynamically over timesteps.
- **Tight correlation with outputs:** Both the visualized difference maps and channel-wise error slices reveal that the error patterns are highly aligned with the generated structures (e.g., feather edges of the bird, textures of the petals). This suggests that quantization errors are not random noise but are strongly coupled with the model outputs, particularly in regions rich in details. This observation is consistent with Output-Correlated Error Propagation, where errors propagate in tandem with the content being generated.
- **Amplification in high-frequency regions:** The difference visualizations further show that quantization errors are most prominent in high-frequency regions such as object boundaries and fine textures. This demonstrates that the statistical correlation of errors with outputs is concentrated on high-frequency components, which are critical for perceptual quality.

G ABLATION EXPERIMENT OF REGULARIZATION TERM λ_1

As shown in Eq. 15, the parameter λ_1 serves to restrict the magnitude of the error correction coefficient, functioning as a regularization term. Moreover, to ensure that $\mathcal{L}(\mathbf{K})$ is a strictly convex

function with respect to K , it is imperative that $\lambda_1 > 0$. We determined the calculation strategy for the λ_1 value through practical comparative experiments. As shown in the Table 6, the grid search strategy does not exhibit any performance advantage over the empirical rule $\lambda_1 = 0.01 \times \frac{\text{mean}(\mu^2)}{\text{var}(\mu)}$, and it has two drawbacks: (1) The grid search strategy requires setting a value range and the number of grid search steps, which incurs significant tuning costs for different models. (2) The grid search strategy needs to repeatedly calculate Eq. 17 multiple times, whereas the empirical rule only requires a single calculation. Therefore, we ultimately adopted the empirical rule to determine the value of λ_1 . Essentially, the empirical rule is a formula-based fitting based on experimental data.

Table 6: Ablation experiment on the selection of regularization term λ_1

Model	Method	FID \downarrow	IR \uparrow	LPIPS \downarrow	PSNR \uparrow
SDXL	SVDQuant (W8A8)	16.6	0.718	0.119	26.4
	TCEC (grid search)	16.2	0.723	0.090	27.1
	TCEC (empirical rule)	16.0	0.728	0.092	27.3

H THE IMPACT OF INFERENCE STEPS ON TCEC PERFORMANCE

Table 1 presents the performance improvements on SDXL-Turbo (4-step), showing that TCEC is likewise applicable to high-speed generative models. However, it is important to note that the gains on SDXL-Turbo are smaller than those on SDXL (50-step). The core reason is that the primary value of TCEC lies in mitigating the accumulation of quantization errors during iterative inference, and thus its performance gains scale directly with the amount of accumulated error. The relatively modest improvements on SDXL-Turbo (4-step) stem from the fact that the small number of steps prevents errors from forming substantial accumulation. Therefore, taking SDXL-Turbo as the baseline, we further conducted additional experiments to investigate the minimal effective number of steps for TCEC.

Table 7: Comparison of SVDQuant and SVDQuant+TCEC across models and steps on MJHQ dataset.

Model	Step	Method	FID \downarrow	PSNR \uparrow	FID \downarrow	PSNR \uparrow	Avg
SDXL	50	SVDQuant	16.6	26.4	-	-	-
		SVDQuant+TCEC	16.0	27.3	0.6	0.9	1.5
SDXL-Turbo	4	SVDQuant	24.3	24.0	-	-	-
		SVDQuant+TCEC	24.5	24.9	-0.2	0.9	0.7
SDXL-Turbo	3	SVDQuant	25.8	18.6	-	-	-
		SVDQuant+TCEC	25.6	18.9	0.2	0.3	0.5
SDXL-Turbo	2	SVDQuant	27.7	17.1	-	-	-
		SVDQuant+TCEC	27.7	17.3	0	0.2	0.2

As shown in Table 7, when the number of iterative steps is ≥ 3 , TCEC produces meaningful improvements (with gains ≥ 0.5 on key metrics). When the number of steps is < 3 , the improvements are constrained by the limited amount of accumulated error and are typically < 0.2 (within the range of experimental noise).

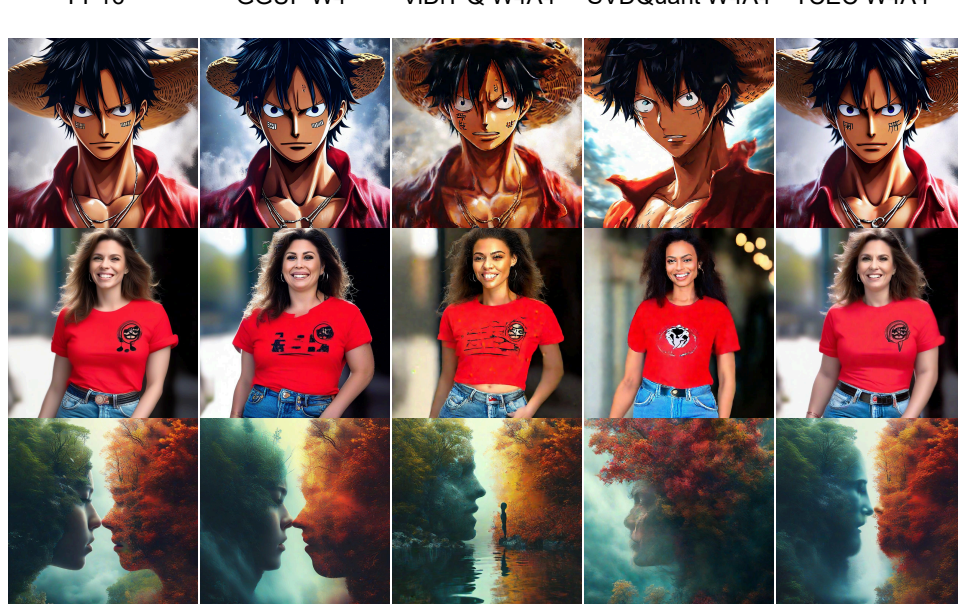
I INFERENCE OVERHEAD OF TCEC

TCEC improves performance by performing error correction on the output of the quantized model, and it is completely orthogonal to the backbone quantization algorithm. As shown in Eq. 14, the computation of single-step quantization error involves no complex operations and is accomplished solely through a non-linear mapping: $\varepsilon_t = \mathbf{K}_t \odot \tilde{\mu}_\theta(\tilde{x}_t, t)$, where \mathbf{K}_t denotes a timestep-conditioned channel-wise scaling matrix, and \odot represents element-wise multiplication. Consequently, the additional theoretical computational complexity introduced at each step is NC^2HW , which is negligible

972 compared to that of the DIT/Unet-Backbone. Practical test data on the Nvidia A800-40G platform
 973 show in Table 8 and Table 3 that the extra end-to-end latency incurred is less than 0.5%, with specific
 974 test data provided in the table below.
 975

976 **Table 8: A comparison of inference overhead between SVDQuant and SVDQuant with TCEC.**

978 Model	978 FP16	978 SVDQuant W4A4	978 SVDQuant+TCEC W4A4
979 Flux-dev 1.0 (T = 30)	979 26.14 s	979 9.947 s	980 9.996 s

981 **J VISUAL QUALITY RESULTS.**

1006 Figure 4: Qualitative visual results comparison. **Prompt1:** *Luffy from ONEPIECE, handsome face, fantasy.* **Prompt2:** *The image features a woman wearing a red shirt with an icon. She appears to be posing for the camera, and her outfit includes a pair of jeans. The woman seems to be in a good mood, as she is smiling. The background of the image is blurry, focusing more on the woman and her attire.* **Prompt3:** *Bright scene, aerial view, ancient city, fantasy, gorgeous light, mirror reflection, high detail, wide angle lens.*

1013 **K CALIBRATION DATASET ABLATION**

1016 To further verify the impact of the calibration dataset on TCEC performance, we provide an explanation
 1017 from both theoretical and experimental perspectives.

- 1018 • **Rationale for selecting the calibration dataset:** The size of the calibration set is chosen
 1019 based on a trade-off between performance and efficiency. As show in Table 9, using
 1020 SVDQuant-W8A8 as the base quantization algorithm, with COCO as the calibration set
 1021 and MJHQ as the evaluation set, the results shown in the table indicate that when the cal-
 1022 ibration set contains fewer than 1024 samples, increasing the number of samples leads to
 1023 significant performance improvements. However, when the calibration set exceeds 1024
 1024 samples and reaches 2048, performance gains plateau. Excessive calibration samples pro-
 1025 vide no additional benefit and instead prolong the calibration process. Therefore, we select
 1026 1024 samples as the standard calibration set size in image generation task.

1026
 1027
 1028
 1029
 1030
 1031
 1032
 1033
 1034
 1035
 1036
 1037
 1038

- **TCEC is insensitive to the domain of the calibration dataset:** The input to TCEC’s error-calibration module is the output of the DiT model, which has already undergone the following processing pipeline: 3D-VAE preprocessing → 3D-VAE Encoder inference → DiT inference. The 3D-VAE preprocessing standardizes the input-output distribution, and the subsequent VAE Encoder and DiT inference further reinforce this effect. As a result, the output distributions of the DiT model converge across different datasets, making the error-correction coefficients largely insensitive to the choice of calibration data. In Table 2, OpenSora uses WebVid as the calibration set and VBench—a dataset with markedly different scenes—for evaluation. Despite the domain shift, TCEC consistently improves performance (e.g., +2.08 on W8A8 Imaging Quality and +3.90 on W4A4), providing direct evidence of its robustness to distributional differences.

Table 9: Performance comparison of SDXL with SVDQuant and TCEC at different data sizes.

	Method	Data Size	FID↓	PSNR↑	FID ↓	PSNR↑	Avg
SDXL	SVDQuant	-	16.6	26.4	-	-	-
	SVDQuant+TCEC	2048	16.0	27.4	0.6	1.0	1.6
	SVDQuant+TCEC	1024	16.0	27.3	0.6	0.9	1.5
	SVDQuant+TCEC	512	16.2	26.8	0.4	0.4	0.8
	SVDQuant+TCEC	256	16.4	26.7	0.2	0.3	0.5

1046
 1047
 1048
 1049
 1050
 1051
 1052
 1053
 1054
 1055
 1056
 1057
 1058
 1059
 1060
 1061
 1062
 1063
 1064
 1065
 1066
 1067
 1068
 1069
 1070
 1071
 1072
 1073
 1074
 1075
 1076
 1077
 1078
 1079